Applied Physics Letters

RESEARCH ARTICLE | JUNE 07 2022

# High-performance non-fullerene acceptor inverted organic photovoltaics incorporating solution processed doped metal oxide hole selective contact

Apostolos Ioakeimidis ; Alina Hauser; Michael Rossier; Flavio Linardi ; Stelios A. Choulis



*Appl. Phys. Lett.* 120, 233301 (2022)
https://doi.org/10.1063/5.0091671







AIP Publishing

Applied Physics Letters ARTICLE scitation.org/journal/apl

# High-performance non-fullerene acceptor inverted organic photovoltaics incorporating solution processed doped metal oxide hole selective contact

Cite as: Appl. Phys. Lett. **120**, 233301 (2022); doi: 10.1063/5.0091671
Submitted: 16 March 2022 · Accepted: 26 May 2022 ·
Published Online: 7 June 2022



Apostolos Ioakeimidis,[1] Alina Hauser,[2] Michael Rossier,[2] Flavio Linardi,[2] and Stelios A. Choulis[1,a)]

## AFFILIATIONS

[1]Molecular Electronics and Photonics Research Unit, Department of Mechanical Engineering and Materials Science and Engineering, Cyprus University of Technology, Limassol 3603, Cyprus
[2]Avantama AG, Laubisruetistr. 50, Staefa 8712, Switzerland

[a)]Author to whom correspondence should be addressed: stelios.choulis@cut.ac.cy

## ABSTRACT

Inverted organic photovoltaics (OPVs) allow flexibility on designing a roll-to-roll production process of OPVs, providing technological opportunities. The OPV roll-to-roll production process demands thick and high-performance solution-based hole selective contacts. Here, we show that a solution processed antimony-doped tin oxide (ATO) hole selective contact produced by spray pyrolysis route exhibits exceptional optoelectronic properties and functionality within non-fullerene acceptor PM6:Y6:$PC_{70}BM$ inverted OPVs. The corresponding solution processed inverted OPVs provide high power conversion efficiency values when a thick hole selective contact of solution processed doped ATO is incorporated within the inverted OPV device structure and similar light stability to that achieved with the commonly used thermally evaporated $MoO_3$ hole selective contact.





Non-fullerene acceptors (NFAs) based electronic materials have been boosting the power conversion efficiency (PCE) for single junction bulk heterojunction organic photovoltaics (OPVs) at the range of 19%.[1,2] This key step creates the potential for commercialization of this photovoltaic technology, which exhibits some distinct advantages compared to the well-established Si-based photovoltaics.[3] An important requirement for the commercial viability of OPVs is the large scale fabrication via roll-to-roll (R2R) printing methods for various layers of the OPV devices.[4,5] Several reports have proven the feasibility of large scale processing of NFA organic active layers.[6] The development of solution processed charge selective contacts plays also a crucial role for achieving high-performance OPVs, in particular for the inverted OPV structure, which provides improved OPV stability.[7–11]

In principle, the selection of charge selective contacts (HSCs) must be assessed based on their reliability, environmental robustness, and process versatility. Metal oxides fulfill the aforementioned requirements and can provide excellent optoelectronic properties, low fabrication cost, and chemical/moisture resistance.[12–14] With respect to the proper selection of the hole selective contact (HSC) for inverted OPVs, certain prerequisites have to be satisfied, such as the low contact resistance and the lowest possible reactivity, while for solution processed HSCs, additional requirements are the complete wettability of the functional organic underlayer and the low thermal annealing temperature.

In the vast majority, the HSC for inverted OPVs is formed by thermal evaporation of thin $MoO_3$ hole transporting layers or by applying solution processed PEDOT:PSS. The low electrical conductivity of $MoO_3$ restricts the acceptable thickness to 10–15 nm. In addition, the introduction of a thermal evaporation step in the fabrication process induces a higher cost and disturbs the roll-to-roll printing process. With regard to the much higher conductive solution processed PEDOT:PSS, even though it fulfills large scale requirements, the sensitivity toward oxygen and moisture negatively affects the long term stability of the devices.[14–16] Solution processed metal oxides such as $WO_3$, $MoO_3$, NiO, and $V_2O_5$ have been reported as suitable hole transporting layers in OPVs, but their low electrical conductivity limits

their electronic layer functionality thickness range to some tens of nanometers.[13,17–19] In more sophisticated approaches, Wang *et al.* have proposed a solution processed hybrid $MoO_3$:PEDOT:PSS as an alternative HSC for inverted OPVs. The applied hybrid HSC was spin-coated on top of the P3HT:$PC_{61}BM$ or PTB7:$PC_{61}BM$ active layer with configuration ITO/ZnO/active layer/HSC/Ag, whereas for the reference devices, the HSC was formed by thermally evaporated $MoO_3$.[20] The application of $MoO_3$:PEDOT:PSS as HSC resulted in thickness-insensitive PCE devices for thickness ranging from 30 to 75 nm. The OPV devices with the hybrid HSC and evaporated Ag resulted in similar PCE performance compared to evaporated $MoO_3$ based inverted OPVs. This report also examined the air stability of the unencapsulated devices for various ratios of $MoO_3$ to PEDOT:PSS HSC. The findings indicate that the higher content of $MoO_3$ improves the long-term stability of the devices but leads to lower PCE values, while higher ratios of PEDOT:PSS improved the PCE but negatively affected the long-term stability. Cominetti *et al.* applied a solution processed buffer layer between the active layer and PEDOT:PSS consisting of vanadium and molybdenum polyoxometalate (POM) salts in ITO/ZnO/active layer/HSC/Ag configuration OPVs.[21] The scope was to avoid the unfavorable contact of the examined active layers (PTB7:$PC_{71}BM$, PV2000:PCBM, and PffBT4T:$PC_{71}BM$) with the PEDOT:PSS. The PCE of the OPVs containing PffBT4T:$PC_{71}BM$ and the POM MoPMo was increased compared to reference devices incorporating evaporated $MoO_3$. Also, the PV2000:PCBM based devices using a double layer exhibit better self-lifetime under nitrogen and room temperature compared to $MoO_3$. In another double layer HSC report, Han *et al.* used a bilayer $WO_3$/HSC Solar (derivative of PEDOT:PSS) in an inverted OPV structure configuration ITO/ZnO/SMD2:ITIC-Th/HSCs/Ag.[22] The inverted OPV devices with a double layer exhibit similar PCE values for an HSC thickness range from 50 to 70 nm and delivered a higher PCE of 10.3% compared to single layer HSC devices, which delivered 7.9 and 8.3% for the HSC solar PEDOT:PSS derivative and $WO_3$, respectively.

Doping can increase the electrical conductivity of hole transporting layers and avoid complicated fabrication processes. Doped metal oxides have been extensively used for the fabrication of low temperature solution processed anode and cathode interlayers for solar cells.[23] Sol–gel synthesized antimony (Sb) doped tin dioxides ($SnO_2$) have been shown to increase the electrical conductivity by almost three orders of magnitude retaining the n-type characteristics for doping levels up to 24%, while the transmission coefficient decreases slowly by increasing the doping level. It is also suggested that these sol–gel synthesized Sb:$SnO_2$ properties match with a degenerated semiconducting material even at low temperatures.[24] The E-beam growth Sb:$SnO_2$ revealed an increase in the conductivity up to two orders of magnitude by increasing the annealing temperature to 900 °C with a simultaneously improvement of the optical transmission in the visible range. The authors ascribe the improved conductivity to two shallow impurity states close to the conduction band due to oxygen vacancies and interstitial Sb.[25] Recently, Liu *et al.* have investigated the optoelectronic properties of spray pyrolysis synthesized Sb:$SnO_2$ nanoparticles (np) for various level of Sb doping. They reported that upon 0.5% Sb doping of $SnO_2$, the electron concentration rapidly decreases to $\sim 10^9$, whereas the hole concentration increases to $\sim 10^{13}$ inducing a shift of the work function level from 4.01 to 5.13 eV, changing the material character to p-type. For a 10% doping, the electrical conductivity increases by almost four orders of magnitude close to $10^{-4}$ S/cm with marginal increase in the work function.[26] We have also shown that ATO can be surface modified with polyethyleneimine (PEI) and function as an efficient electron selective contact in P3HT:IDTBR and P3HT:$PC_{60}BM$ based inverted OPVs.[27]

In this report, we demonstrate the application of spray pyrolysis synthesized Sb-doped $SnO_2$ (ATO, 10 mol. % Sb) nanoparticles as a solution processed HSC in PM6:Y6:$PC_{70}BM$ NFA based inverted OPVs. The selection of the PM6:Y6:$PC_{70}BM$ active layer was based on previous reports that demonstrated the enhanced performance of the ternary system in OPV compared to binary PM6:Y6.[28–30] We examine the impact of two different thicknesses of the ATO layer, thin (20 nm) and thick layers (130 nm), fabricated on top of the NFA active layer using doctor blading processing in air. The inverted OPVs incorporating the thick ATO HSC deliver a similar performance to the reference device, which is based on thermally evaporated $MoO_3$, while the thin ATO HSC inverted OPVs provide much lower PCE values. Importantly, the reported light stability tests under one sun simulated light (1.5 A.M.) of unencapsulated inverted OPVs in air show that the $MoO_3$ HSC based inverted OPVs and the thick ATO HCS based inverted OPVs exhibit almost identical rate of degradation. These findings indicate that the thermally evaporated $MoO_3$ can be replaced by a 130 nm solution processable Sb-doped $SnO_2$ (ATO, 10 mol. % Sb) nanoparticle layer within the inverted OPV device architecture, and thus, it can be considered as a high-performance solution processable HSC for NFA-based inverted OPVs.

The 10 mol. % Sb-doped tin oxide (ATO) nanoparticles were prepared by flame spray pyrolysis synthesis route with scalable control parameters. The synthesized nanoparticles were measured to have a primary crystallite size of ~5 nm as determined by XRD measurement, while the PL measurements (Fig. S1) agree with UV-vis absorption spectra.[27] The addition of antimony (Sb) as a dopant for $SnO_2$ was chosen given the relative similarity of the $Sn_4^+$ and the $Sb_3^+$ ionic radii. This similarity allows for substitutional doping of Sb atoms into the $SnO_2$ lattice. Antimony (Sb) is acting as a p-type dopant and, therefore, increases the electrical conductivity as well as the work function of the $SnO_2$ compound.[26] For this study, a 10% antimony (Sb) doped $SnO_2$ was selected due to higher resulting electrical conductivity compared to 5% and 20% doping levels (Fig. S2).

Figure 1(a) illustrates the device structure of the inverted PM6:Y6:$PC_{70}BM$ based OPV with a ~20 nm solution processed ZnO-nanoparticle electron transporting layer used for all the inverted OPVs under investigation, while for the HSC, either a thin (~20 nm) or a thick (~130 nm) hole transporting layer of solution processed ATO was used. The thickness of the ATO films was determined by profilometry measurements (Fig. S3). For the ZnO layer, the Avantama solution (N-10-Flex) was spin-coated on top of prepatterned Indium Tin oxide (ITO) in air. The active layer PM6:Y6:$PC_{70}BM$ (1:1:0.2, 16 mg/ml in chloroform) was spin-coated in air and annealed in the glovebox at 100 °C for 10 min. Then, the ATO ink was bladed coated on a 70 °C heated plate in air using 20 or 80 mm/s blade speed, for the formation either a thin or thick ATO layer, and importantly, no further annealing treatment was applied. To complete the inverted OPVs, the samples were transferred in a high vacuum chamber (HVC) where a 100 nm Ag back contact was thermally evaporated. For comparison, reference inverted OPVs were fabricated with the same architecture,

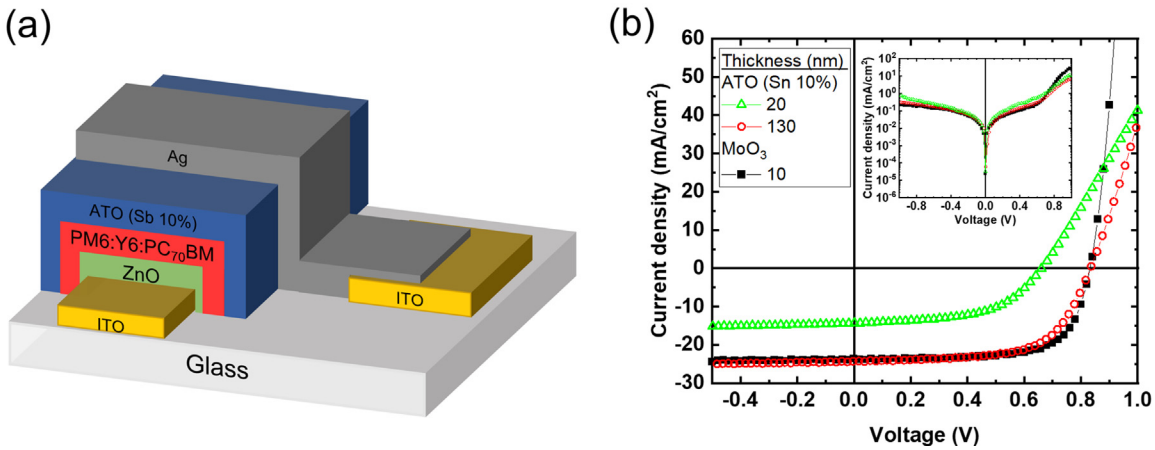


**FIG. 1.** (a) Schematic representation of the inverted PM6:Y6:$PC_{70}BM$ based solar cell architecture and (b) the obtained J–V curves under one sun simulated light (A.M. 1.5) and dark condition (inset) of inverted solar cells incorporating thin or thick ATO HSC and of the reference device with 10 nm thermally evaporated $MoO_3$.

but the ATO-based HSC was replaced by a 10 nm thermally evaporated $MoO_3$ hole transporting layer. Figure 1(b), main plot and inset plot, presents the J–V curves under one sun simulated light (1.5 A.M.) and dark conditions, respectively, of the best performing inverted OPVs incorporating the various HSCs investigated within this paper. The extracted photovoltaic parameters obtained from 32 devices (corresponding to four identical runs with eight devices each) for the inverted solar cells incorporating the HSCs under investigation are presented in Table I.

Comparing the inverted OPV devices incorporating thin (20 nm) and thick ATO (130 nm) HSC, the power conversion efficiency (PCE) of the corresponding inverted OPVs shows difference in distinct performance. Specifically, for the thick ATO hole transporting layer, the mean PCE is 12.48% with a standard deviation (STDV) of 0.40%, while the thin ATO hole transporting layer delivered a much lower mean PCE of 4.90% with STDV 0.25%. The best inverted OPVs incorporating the thick ATO hole transporting layer deliver a PCE of 13.00%, while the thin ATO hole transporting layer based inverted OPVs provided a limited PCE of 5.19%. Focusing on the resultant photovoltaic (PV) parameters $V_{oc}$, $J_{sc}$, and FF, it is observed that the thick ATO HSC delivers a mean $V_{oc}$ of 0.84 V with low variation between the devices (STDV $< 0.01\%$), a high mean $J_{sc}$ of 23.51 mA/cm$^2$ (STDV 0.59 mA/cm$^2$), and a mean FF of 63.19% (STDV 0.44%). On the contrary, all the mean photovoltaic parameters of the inverted solar cells using thin ATO HSC show severe limitations, obtaining $V_{oc} = 0.66$ V (STDV 0.01 V), $J_{sc} = 13.64$ mA/cm$^2$ (STDV 0.39 mA/cm$^2$), and FF = 54.46% (STDV 1.55%). The $J_{sc}$ results obtained by the light J–V characterization are in good agreement (within 5%) with the integrated current densities calculated by the EQE measurements (Fig. S4). The corresponding OPV parameters for the best performing inverted OPVs using the thick and thin ATO HSCs follow similar trend with the mean values, which are clearly depicted in the respective J–V curves [Fig. 1(b)]. The dark curves of the corresponding devices are shown in the inset of Fig. 1(b). The thin ATO HSC based inverted OPVs show a higher dark current due to penetrated metal through the insufficient thick ATO hole transporting layer, resulting in limited PCE parameters. On the contrary, the thicker solution processed ATO HSC (130 nm) shows similar dark current for the region −1.0 V up to turn-on voltage. At higher forward biases, the thick ATO HSC based inverted OPVs exhibit a lower rectification ratio and higher series resistance compared to reference thermally evaporated $MoO_3$ hole transporting layer based inverted OPVs, which is correlated with the lower mean FF obtained from the light J–V characterization.

The thick 130 nm ATO HSC based inverted OPVs provide a PCE, which approximates the value of the reference 10 nm thermally evaporates $MoO_3$ HSC based inverted OPVs. The delivered mean PCE of the reference thermally evaporates $MoO_3$ inverted OPV is 12.99% (STDV 0.34%) with the PCE relative difference being only ∼4% compared to the proposed inverted OPVs incorporating thick (130 nm) solution processed ATO HSC. With respect to the respective mean PV parameters for both batch of inverted OPVs, we obtain $V_{oc}$ 0.84 V and similar $J_{sc}$ (23.59 and 23.51 mA/cm$^2$), with the reference

**TABLE I.** The resulting inverted solar cells power conversion efficiency parameter [mean PCE performance (and best PCE performing devices in parenthesis)] incorporating 20 or 130 nm ATO HSC, respectively, and the reference device with 10 nm thermally evaporated $MoO_3$.

| ATO | $V_{oc}$ (V) | STDV | $J_{sc}$ (mA/cm$^2$) | STDV | FF (%) | STDV | PCE (%) | STDV |
|---|---|---|---|---|---|---|---|---|
| 20 nm | 0.66 (0.66) | 0.01 | −13.64 (−14.35) | 0.39 | 54.46 (54.75) | 1.55 | 4.90 (5.19) | 0.25 |
| 130 nm | 0.84 (0.84) | 0 | −23.51 (−24.36) | 0.59 | 63.19 (63.62) | 0.44 | 12.48 (13.00) | 0.40 |
| $MoO_3$ | $V_{oc}$ (V) | STDV | $J_{sc}$ (mA/cm$^2$) | STDV | FF (%) | STDV | PCE (%) | STDV |
| 10 nm | 0.84 (0.84) | 0 | −23.59 (−23.14) | 0.49 | 68.83 (70.30) | 1.82 | 12.99 (13.66) | 0.34 |

$MoO_3$ inverted OPVs exhibiting a slightly higher FF of 68.83% compared to 63.19% of the thick ATO HSC based inverted OPVs. Nevertheless, the similarity in the efficiency performance mean values is impressive, given that the reference inverted OPVs incorporate a high precision/cost deposition technique (thermal evaporation) for the 10 nm $MoO_3$ in contrast to the rougher solution/low-cost process technique (blade coating) applied for the fabrication of the 130 nm ATO HSC.

The similar PCE values obtained for the reference thermally evaporated $MoO_3$ HSC based inverted OPVs and thick solution processed ATO HSC based inverted OPVs originate from the ability of the doped ATO to function as an efficient HSC even for thick layers. This advantage is ascribed to (1) the relatively high electrical conductivity $10^{-3}$ S/cm (four-point probe measurement), (2) high transparency even for thick layers [Fig. 2(a)] since transparency for the thick ATO hole transporting layer is reduced by less than 5% at the spectral region 400–800 nm compared to the thin ATO hole transporting layer, and (3) the capability of fabricating smooth and compact hole transporting layers for both the thin and thick ATO layer as shown in AFM pictures [Figs. 2(c) and 2(d)] enabled by the low contact angle (6.9°) of the ATO ink on the active layer [Fig. 2(b)]. The similar roughness of 9.6 and 9.3 nm and the similar range of phase shift (Fig. S4) for the thin and thick ATO, respectively, indicate that both layers fully covered the active layer.

Since both the thin and thick ATO hole transporting layers are compact, we can infer that the lower PCE values of the thin based devices are related to the Ag metal evaporation process. Due to the nanoparticulate nature of the solution processed ATO hole transporting layers, the Ag ions diffuse through the thin ATO HSC contacting the underlying NFA active layer resulting in reduced PV parameters.[31–33] The degradation is ATO HSC thickness dependence, a parameter that makes chemical interactions unlikely and clearly indicate diffusion of top metal Ag related degradation, which can be inhibited by the proposed thick ATO HSC acting as a diffusion blocking layer.

The light stability of unencapsulated inverted OPVs was investigated under one sun (A.M. 1.5) solar simulated light in ambient conditions. Between J–V characterization, the inverted OPV devices were hold at $V_{oc}$ potential under light. Figure 3 presents the relative change of the PV parameters of optimized inverted PM6:Y6:$PC_{70}BM$ OPVs (bars represent the relative STDV) with thin and thick ATO HSC. In addition, we provide preliminary results on the light stability of inverted OPV devices incorporating thin and thick ATO HSC for a range of NFA acceptor based active layers. Figures S5–S7 show the relative change of PCE in air under one sun simulated light for the inverted OPVs incorporating PM6:Y6, PM6:PY6:IDTBR, and P3HT:IDTBR active layers, respectively. As observed in Figs. S5–S7, thick ATO HSC has a positive impact on the light stability for all the investigated inverted OPVs. Nevertheless, the impact of the proposed thick ATO HSC on lifetime performance is different for the various active layers. As we discussed above, wetting properties and the ability to process thick ATO HSC contact depend on the undercoated active



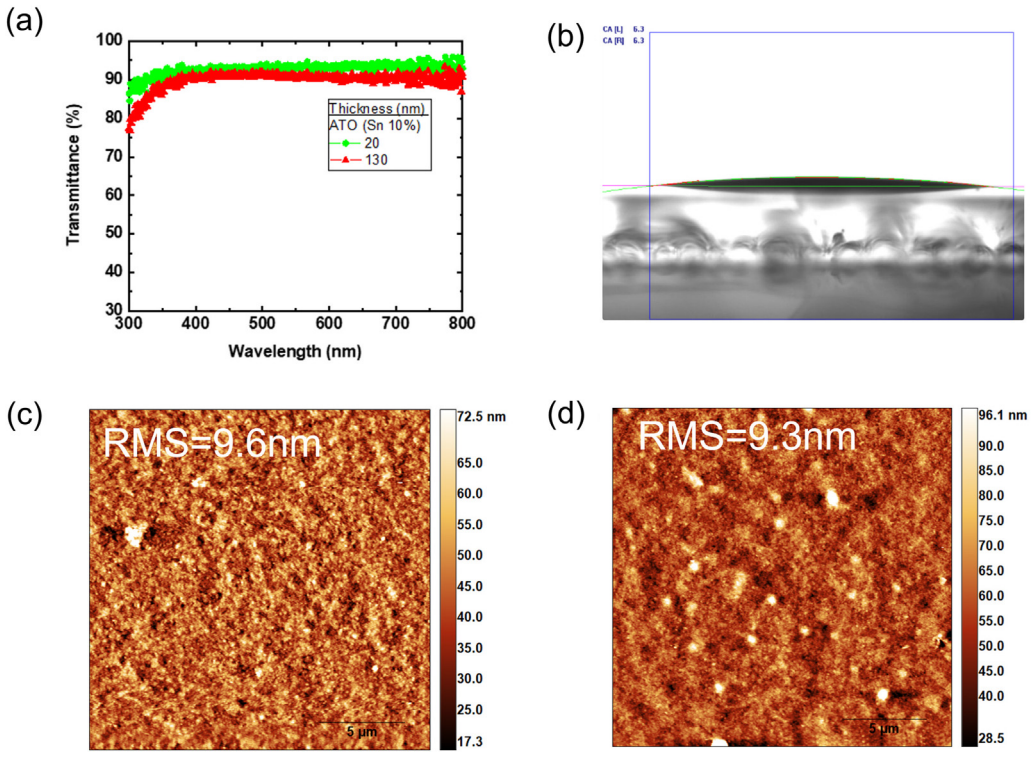


**FIG. 2.** (a) Optical transmittance of thin and thick ATO layers fabricated on top of quartz substrate. (b) Contact angle (6.3°) of the ATO ink on top of the PM6:Y6:$PC_{70}BM$ layer. AFM images obtained for (c) thin and (d) thick ATO on top of PM6:Y6:$PC_{70}BM$.

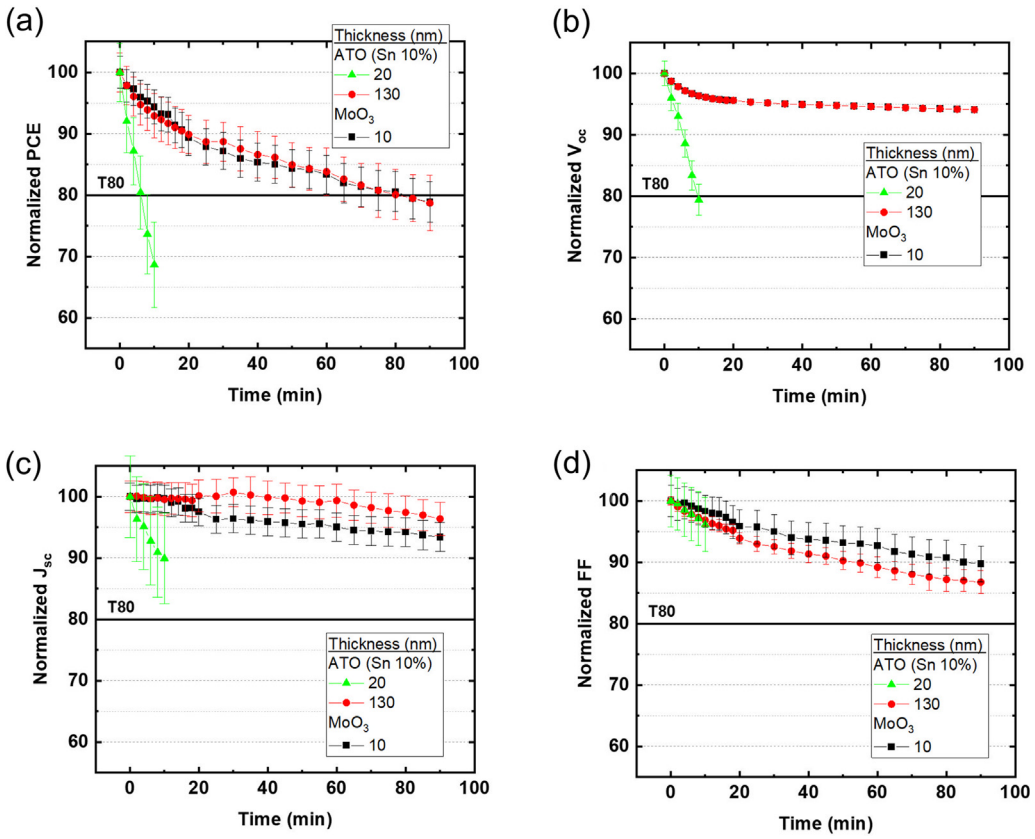


**FIG. 3.** Time dependent evolution of (a) PCE, (b) $V_{oc}$, (c) $J_{sc}$, and (d) FF of the unencapsulated inverted PM6:Y6:$PC_{70}BM$ based OPV cell in air under one sun simulated light, for devices incorporating solution processed thin or thick ATO HSC against the reference device incorporating thermally evaporated $MoO_3$.

layers; furthermore, possible photochemical reactivity between ATO HSC and active layers might influence the lifetime performance of thick ATO hole selective contact, and such parameters have to be addressed/optimized in detail depending on the active layer.

For the optimized PM6:Y6:$PC_{70}BM$ inverted OPVs, which is the focus of this study, the thin ATO based PM6:Y6:$PC_{70}BM$ OPVs exhibits a similarly steep decline of the PCE within the first few minutes after the light exposure [Fig. 3(a)]. The $V_{oc}$ having the higher contribution on the PCE reduction reaches the 80% of the initial value within the first ten minutes of investigation. The other two PV parameters ($J_{sc}$ and FF) show a slower decline [Figs. 3(c) and 3(d)] compared to $V_{oc}$, yet the $J_{sc}$ reduction rate is faster than the reference thermally evaporated $MoO_3$ based inverted OPVs. Importantly, the inverted PM6:Y6:$PC_{70}BM$ OPVs incorporating thick (130 nm) ATO HSC and the reference inverted OPVs incorporating thermally evaporated $MoO_3$ exhibit almost identical PCE light degradation rates, reaching the 80% of the initial PCE performance after about 80 min. The degradation of the $V_{oc}$ is identical for the thick solution processed ATO HSC based inverted OPVs and reference thermally evaporated $MoO_3$ based inverted OPVs, showing a typical fast initial degradation, and then the degradation rate becomes much slower. The $J_{sc}$ and FF exhibit opposite behavior for the thick ATO HSC based inverted OPVs and the reference thermally evaporated $MoO_3$ based inverted OPVs, with the former exhibiting a slower degradation of the $J_{sc}$ but faster degradation of the FF compared to the reference thermally evaporated $MoO_3$ based inverted OPVs. For both batches of inverted OPVs under investigation, the FF shows the higher decline compared to the other PV parameters within the investigated light lifetime time scales. Thus, the solution processed thick (130 nm) ATO HSC based inverted OPVs demonstrate a comparable PCE and light stability performance with the commonly used thermally evaporated $MoO_3$ HSC based inverted OPVs.

To conclude, inverted solution processed NFA based OPVs offer the promise of a low-cost, roll-to-roll printed solar PV technology. Solution processable Sb-doped $SnO_2$ (ATO, 10 mol. % Sb) metal oxide ink processed on the top of the PM6:Y6:$PC_{70}BM$ NFA organic active layer by doctor-blading processing temperature of 70 °C and without the requirement of any further annealing step exhibits exceptional wetting properties, electrical conductivity, optical transmittance, and hole charge carrier selectivity, which are critical parameters for efficient solution processed HSCs in inverted OPVs. Device implementation reveals that 130 nm thick ATO is an ideal solution-based HSC for inverted PM6:Y6:$PC_{70}BM$ OPVs providing similar PCE and light stability performance to that achieved with the commonly used thermally evaporated $MoO_3$ HSC. This work is a step forward in resolving one of the most important research and development challenges in the

field of inverted OPVs by providing a low temperature solution processed metal oxide HSC suitable for PM6:Y6:$PC_{70}BM$ NFA inverted OPVs printing technology requirements.

See the supplementary material for details of materials, devices fabrication, and characterization techniques and also for additional figures for PL, four-point probe, profilometry, EQE, AFM phase image measurements, light stability measurements of PM6:Y6, PM6:Y6:IDTBR, and P3HT:IDTBR inverted OPV devices.

The authors acknowledge the funding from the European Union's Horizon 2020 research and innovation program under Grant Agreement No. 862474 (project RoLA-FLEX).

## AUTHOR DECLARATIONS

### Conflict of Interest

The authors have no conflicts to disclose.

### Author Contributions

**Apostolos Ioakeimidis:** Data curation (equal); Formal analysis (equal); Investigation (equal); Methodology (equal); Writing – original draft (equal); Writing – review & editing (equal). **Alina Hauser:** Formal analysis (equal); Investigation (equal); Methodology (equal); Writing – review & editing (equal). **Michael Rossier:** Formal analysis (equal); Investigation (equal); Methodology (equal); Supervision (equal). **Flavio Linardi:** Data curation (equal); Formal analysis (equal); Investigation (equal). **Stelios A. Choulis:** Conceptualization (equal); Formal analysis (equal); Funding acquisition (equal); Investigation (equal); Methodology (equal); Supervision (equal); Writing – original draft (equal); Writing – review & editing (equal).

## DATA AVAILABILITY

The data that support the findings of this study are available from the corresponding author upon reasonable request.

## REFERENCES

[1]S. Bao, H. Yang, H. Fan, J. Zhang, Z. Wei, C. Cui, and Y. Li, Adv. Mater. **33**, 2105301 (2021).
[2]C. Yan, S. Barlow, Z. Wang, H. Yan, A. K. Y. Jen, S. R. Marder, and X. Zhan, Nat. Rev. Mater. **3**, 18003 (2018).
[3]Y. Tong, Z. Xiao, X. Du, C. Zuo, Y. Li, M. Lv, Y. Yuan, C. Yi, F. Hao, Y. Hua, T. Lei, Q. Lin, K. Sun, D. Zhao, C. Duan, X. Shao, W. Li, H. L. Yip, Z. Xiao, B. Zhang, Q. Bian, Y. Cheng, S. Liu, M. Cheng, Z. Jin, S. Yang, and L. Ding, Sci. Sin-Chim. **50**, 437 (2020).
[4]M. Riede, D. Spoltore, and K. Leo, Adv. Energy Mater. **11**, 2002653 (2021).
[5]H. Liu, M. H. Yu, C. C. Lee, X. Yu, Y. Li, Z. Zhu, C. C. Chueh, Z. Li, and A. K. Y. Jen, Adv. Mater. Technol. **6**, 2000919 (2021).
[6]A. S. Gertsen, M. F. Castro, R. R. Søndergaard, and J. W. Andreasen, Flexible Printed Electron. **5**, 014004 (2020).
[7]R. Steim, S. A. Choulis, P. Schilinsky, and C. J. Brabec, Appl. Phys. Lett. **92**, 093303 (2008).
[8]C. Waldauf, M. Morana, P. Denk, P. Schilinsky, K. Coakley, S. A. Choulis, and C. J. Brabec, Appl. Phys. Lett. **89**, 233517 (2006).
[9]J. A. Hauch, P. Schilinsky, S. A. Choulis, R. Childers, M. Biele, and C. J. Brabec, Sol. Energy Mater. Sol. Cells **92**, 727 (2008).
[10]C.-Y. Li, T.-C. Wen, T.-H. Lee, T.-F. Guo, J.-C.-A. Huang, Y.-C. Lin, and Y.-J. Hsu, J. Mater. Chem. **19**, 1643 (2009).
[11]Y. Li, X. Huang, K. Ding, H. K. M. Sheriff, L. Ye, H. Liu, C.-Z. Li, H. Ade, and S. R. Forrest, Nat. Commun. **12**, 3049 (2021).
[12]M. Yi, S. Hong, J. R. Kim, H. Kang, J. Lee, K. Yu, S. Kee, W. Lee, and K. Lee, Sol. Energy Mater. Sol. Cells **153**, 117 (2016).
[13]H. N. Tran, D. Q. Dao, Y. J. Yoon, Y. S. Shin, J. S. Choi, J. Y. Kim, and S. Cho, Small **17**, 2101729 (2021).
[14]R. Sorrentino, E. Kozma, S. Luzzati, and R. Po, Energy Environ. Sci. **14**, 180 (2021).
[15]N. Ahmad, H. Zhou, P. Fan, and G. Liang, EcoMat **4**, e12156 (2022).
[16]S. Park, T. Kim, S. Yoon, C. W. Koh, H. Y. Woo, and H. J. Son, Adv. Mater. **32**, 2002217 (2020).
[17]C. P. Chen, Y. D. Chen, and S. C. Chuang, Adv. Mater. **23**, 3965 (2011).
[18]T. Stubhan, N. Li, N. A. Luechinger, S. C. Halim, G. J. Matt, and C. J. Brabec, Adv. Energy Mater. **2**, 1433 (2012).
[19]F. Güzelçimen, H. Ibrahim, Y. Ozen, and S. Ozçelik, Opt. Mater. **120**, 111457 (2021).
[20]Y. Wang, Q. Luo, N. Wu, Q. Wang, H. Zhu, L. Chen, Y. Q. Li, L. Luo, and C. Q. Ma, ACS Appl. Mater. Interfaces **7**, 7170 (2015).
[21]A. Cominetti, G. Serrano, A. Savoini, C. Carbonera, F. Melchiorre, S. Perucchini, A. Congiu, G. Corso, R. Barbieri, E. Trippodo, A. Caneschi, and R. Po, Phys. Status Solidi A **217**, 1901023 (2020).
[22]Y. W. Han, S. J. Jeon, H. S. Lee, H. Park, K. S. Kim, H. W. Lee, and D. K. Moon, Adv. Energy Mater. **9**, 1902065 (2019).
[23]Q. Luo, in *Solutions Processed Metal Oxide Thin Films for Electronic Applications*, edited by Z. Cui and E. A. Korotcenkov (Elsevier, 2020), pp. 109–140.
[24]C. Terrier, J. P. Chatelon, and J. A. Roger, Thin Solid Films **295**, 95 (1997).
[25]Y.-S. He, J. C. Campbell, R. C. Murphy, M. F. Arendt, and J. S. Swinnea, J. Mater. Res. **8**, 3131 (1993).
[26]C. Liu, R. Félix, K. Forberich, X. Du, T. Heumüller, G. J. Matt, E. Gu, J. Wortmann, Y. Zhao, Y. Cao, Y. He, L. Ying, A. Hauser, M. F. Oszajca, B. Hartmeier, M. Rossier, N. A. Lüchinger, Y. Liu, J. Guo, K. Nie, R. G. Wilks, J. Bachmann, M. Bär, N. Li, and C. J. Brabec, Nano Energy **89**, 106373 (2021).
[27]E. Georgiou, I. T. Papadas, I. Antoniou, M. F. Oszajca, B. Hartmeier, M. Rossier, N. A. Luechinger, and S. A. Choulis, APL Mater. **7**, 091103 (2019).
[28]M.-A. Pan, T.-K. Lau, Y. Tang, Y.-C. Wu, T. Liu, K. Li, M.-C. Chen, X. Lu, W. Ma, and C. Zhan, J. Mater. Chem. A **7**, 20713 (2019).
[29]T. Yan, W. Song, J. Huang, R. Peng, L. Huang, and Z. Ge, Adv. Mater. **31**, 1902210 (2019).
[30]A. Distler, C. J. Brabec, and H. J. Egelhaaf, Prog. Photovoltaics Res. Appl. **29**, 24 (2021).
[31]Z. Huai, L. Wang, Y. Sun, R. Fan, S. Huang, X. Zhao, X. Li, G. Fu, and S. Yang, ACS Appl. Mater. Interfaces **10**, 5682 (2018).
[32]V. I. Madogni, B. Kounouhéwa, A. Akpo, M. Agbomahéna, S. A. Hounkpatin, and C. N. Awanou, Chem. Phys. Lett. **640**, 201 (2015).
[33]N. Chaturvedi, N. Gasparini, D. Corzo, J. Bertrandie, N. Wehbe, J. Troughton, and D. Baran, Adv. Funct. Mater. **31**, 2009996 (2021).